PAPER

Segmentation-free image processing and analysis of precipitate shapes in 2D and 3D

To cite this article: Ben Bales *et al* 2017 *Modelling Simul. Mater. Sci. Eng.* **25** 045009

IOP Publishing Modelling and Simulation in Materials Science and Engineering
Modelling Simul. Mater. Sci. Eng. **25** (2017) 045009 (12pp) https://doi.org/10.1088/1361-651X/aa67b9

Segmentation-free image processing and analysis of precipitate shapes in 2D and 3D

Ben Bales[1], **Tresa Pollock**[2] **and Linda Petzold**[1]

[1] Department of Mechanical Engineering, University of California, Santa Barbara, CA 93106-5070, United States of America
[2] Materials Department, Engineering II Building, 1355 University of California, Santa Barbara, Santa Barbara, CA 93106-5050, United States of America

E-mail: bbbales2@gmail.com

Received 3 November 2016, revised 5 March 2017
Accepted for publication 20 March 2017
Published 19 April 2017

Abstract

Segmentation based image analysis techniques are routinely employed for quantitative analysis of complex microstructures containing two or more phases. The primary advantage of these approaches is that spatial information on the distribution of phases is retained, enabling subjective judgements of the quality of the segmentation and subsequent analysis process. The downside is that computing micrograph segmentations with data from morphologically complex microstructures gathered with error-prone detectors is challenging and, if no special care is taken, the artifacts of the segmentation will make any subsequent analysis and conclusions uncertain. In this paper we demonstrate, using a two phase nickel-base superalloy microstructure as a model system, a new methodology for analysis of precipitate shapes using a segmentation-free approach based on the histogram of oriented gradients feature descriptor, a classic tool in image analysis. The benefits of this methodology for analysis of microstructure in two and three-dimensions are demonstrated.

Keywords: microstructure analysis, rafting, feature descriptor

(Some figures may appear in colour only in the online journal)

1. Introduction

The strong driving force for development of rigorous property models for structural materials motivates quantitative analysis of microstructure across a spectrum of alloy systems [1]. Since most engineering materials are multiphase in character, it is usually essential to isolate individual phases for analysis of size, shape and/or distribution in order to input this information into property models. The process for quantifying microstructure typically involves

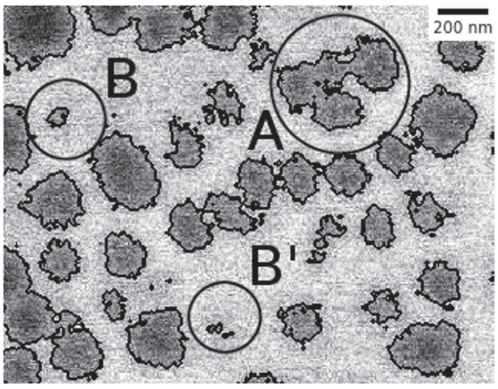

Figure 1. An example backscattered electron micrograph showing γ matrix (light) and γ' precipitates (dark). *A*, *B*, and *B*′ highlight regions where the presence of a precipitate is uncertain. *A* shows four precipitates that have been incorrectly merged by the segmentation algorithm. *B* and *B*′ highlight areas where maybe there is a precipitate and maybe there is not. In both cases the segmentation algorithm must make a decision between these two extremes.

collection of 2D or 3D data on a pixel by pixel basis, followed by a segmentation operation to isolate individual phases within the microstructure. Shape metrics such as volumes, surface areas, or statistical moments [2, 3]) of the resulting precipitates are used to quantify the analysis. These metrics are chosen in part because of their similarity with quantitative microstructure analysis that has been performed manually [4, 5]. The conjecture is that if enough micrographs can be captured and enough precipitates can be characterized, the shape statistics will yield good feature descriptors that can then be used in whatever classification or regression tasks that need to be addressed.

The examples in this paper are of nickel-based superalloys. For these alloys, it is desirable to develop heat treatment cycles to adjust precipitate shapes for optimization of mechanical properties [4]. A unique feature of this class of alloys is the tendency for the precipitates to undergo directional coarsening during the application of external stresses at elevated temperatures [6], a process known as 'rafting'. In both cases, measuring the shape of the microstructural precipitates can provide important insights on alloy design and mechanical properties.

The problem with this measurement is that the segmentations are rarely trivial. Especially across data sets, but even within datasets, it can be very difficult to parameterize a segmentation algorithm to produce consistent results. Because the segmentation parameterization can strongly influence the shape statistics and because producing high quality segmentation often requires extensive fine tuning of segmentation parameters, it is difficult to argue that the resultant shape statistics are unbiased (with regards to the segmentation). The artifacts an automated segmentation of a γ–γ' microstructure might produce depend on the imaging modality, but typically include:

1. A large number of single pixel γ or γ' precipitates appear due to detector noise in the original image.
2. Individual precipitates are merged into one large precipitate because the original image does not have high enough resolution for them to be segmented without high level material-specific knowledge.

Figure 1 shows an example image with the first two types of defects. These issues are not unique to superalloy microstructures, and techniques can be developed to address them [7–10], though it is still very difficult to make them robust, particularly across data sets. The simpler solution, if the information needed and the associated analysis allows, is to employ image analysis approaches that do not rely on segmentation.

The goal of this paper is to highlight how a tool from computer vision, the histogram of oriented gradients (HOGs) feature detector, can be used to solve a wide variety of relevant classification and measurement problems robustly with respect to the difficulties enumerated above. HOG feature detectors have a long, rich history of application in computer vision [11–13], but to the best of our knowledge have not been used in the study of microstructure.

This paper is organized as follows. In section 2 we describe related work and in section 3 we outline computation of a HOG feature descriptor. In section 4 we demonstrate the effectiveness of the HOG feature descriptor on a number of relevant microstructure characterization problems, where microstructural information is available in both 2D and 3D.

2. Related work

There is an extensive existing literature on microstructure analysis including understanding how composition affects microstructure [6, 14], understanding how processing steps affect microstructure [15], and understanding how precipitate shape properties affect strength [4], etc. Most of these papers use segmentation based characterization techniques, be they measuring simple areas, aspect ratios, and perimeters [5] or more complicated metrics [2, 3].

There are many similarities between microstructure analysis and the classic problem of shape analysis [16, 17]. Shape analysis in general involves taking outlines of objects and using this information, for example in simple object recognition [17] or pose estimation [16]. A frequent limitation in this process was, much like for the microstructures, obtaining the outlines of the objects. Outlining is simply a segmentation, albeit the images are usually much more complicated than a superalloy microstructure micrograph. This field took a leap forward as techniques were developed to solve the motivating problems directly (pose estimation, object recognition, etc), without first doing a segmentation. Even though the idea of a segmentation as a blackbox step in shape analysis seemed reasonable, it was limiting. These changes were fueled by the introduction the scale-invariant feature transforms (SIFTs) [18] for sparse keypoint identification, the repopularization of HOG descriptors by Dalal and Triggs [19], and, more currently, work in neural networks [20]. The inspiration to our current work was the success that shape analysis enjoyed with these segmentation-free feature descriptors. There are, however, reconstruction-based imaging techniques that can directly lead to easier to segment datasets [21, 22] as compared to the simple micrographs used here.

Several other microstructure characterization techniques that do not involve segmentation have recently been employed, including *N*-point statistics [23, 24] and SIFT [25]. What, given the established application of *N*-point statistics and SIFT in microstructure analysis do HOG descriptors provide? Basically, while a quantitative, segmentation-free feature vector is desired, it is also desirable that the feature vectors be easily interpretable by lab scientists. The strength of a segmentation is that the data it produces (the outlines of the precipitates) is easy to directly interpret and understand. Our goal has been to develop a technique that makes both of these scenarios possible: quantitative analysis similar to the *N*-point statistics and SIFT features, and qualitative analysis similar to that done with segmentations. HOG descriptors, as used here, fill that gap. Their computation, interpretation, and analysis are straightforward.

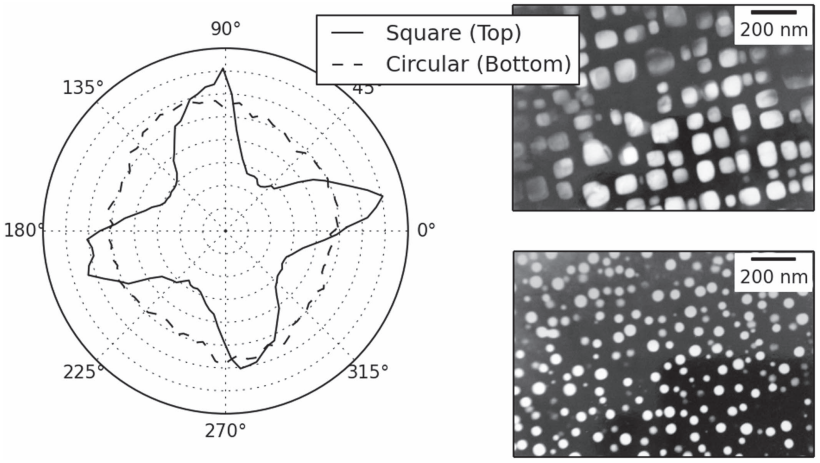

Figure 2. Plot of the HOG feature descriptors (on the left) of transmission electron microscope micrographs of two superalloy samples [14]. As can be seen, the precipitates in the top micrograph are more square than the precipitates in the bottom micrograph. A two pixel blur was used in computing the gradients here.

3. Methods

Computation of the HOG feature descriptor itself is straightforward. This technique is suitable for either standard scanning or tunneling electron microscope micrographs. The HOG feature detector is relatively coarse, and so the micrograph only needs to be of modest size, practically somewhere between 200 × 200 and 1000 × 1000 pixels. First, an approximate gradient at every point in the image is computed. This is most easily done by applying a light Gaussian blur (just a few pixel radii) to the image and taking finite differences to obtain the gradients. The Gaussian kernel should be large enough to remove the largest detector noise, but not so large that it blurs any important features. Finally, the values of the gradient are summed into a histogram of gradient angles weighted by gradient magnitudes.

For image F with Gaussian kernel G, the gradient at each point, f_{ij}, is given by $\nabla(G * F)_{ij}$. f_{ij} is a vector with magnitude $|f_{ij}|$ and angle $\angle f_{ij}$. To build the histogram over angles, if each bin center is denoted as θ_k with radius δ, then the value of the histogram W at that bin center is given by

$$W(\theta_k) = \sum_{|\angle f_{ij} - \theta_k| < \delta} |f_{ij}|. \tag{1}$$

4. The HOG feature detector

4.1. Comparison of microstructures

As stated before, a valuable feature of HOGs is the relative ease of their computation as compared to segmentations. Figure 2 shows the comparison of two superalloy microstructures from Fährmann [14].

As shown in figure 2, the HOG feature descriptor has peaks pointing in the normal directions of the facets in the top sample of figure 2. This is because the histogram

Table 1. Magnitudes of the energies in the bins of the normalized HOG feature vector. As can be seen, the circular microstructure has more energy allocated in its zero bin (highlighted in dark gray), and the square microstructure has more energy in the fourth and eighth bin (highlighted in light gray).

|FFT| of HOG feature descriptors for figure 2								
Square (top)	59	0.46	0.70	0.65	13	1.3	0.70	0.19	2.7
Circle (bottom)	88	1.4	2.9	0.29	2.2	0.32	0.29	0.57	0.18
Index	0	1	2	3	4	5	6	7	8

Table 2. These are the HOG scores for figure 2. As can be seen, the Circle score is much higher for the circular microstructure, and the Square score is much higher for the square microstructure.

HOG scores for figure 2			
	Circle (0 Hz signal)	Square (4 Hz harmonics)	Layering (2 Hz harmonics)
Square (top)	20	0.95	0.97
Circle (bottom)	460	0.29	0.80

accumulates the magnitudes of gradients, so that where the gradient is large, large values are accumulated. In these superalloy micrographs, the gradients are large at the edges of precipitates. The precipitates in the bottom sample are more spherical, and the HOG feature descriptor reflects this.

The simplest way to use the HOG as a quantitative descriptor instead of qualitative descriptor is to look at the magnitude of the FFT of the HOG feature descriptor and compare the relative amount of energy in different harmonics of the microstructure. The first nine bins of the absolute value of the FFTs of the HOG feature descriptors from figure 2 are shown in table 1.

We can compare how circular the precipitates in the two microstructures are by comparing the amount of energy in bin zero of the magnitude of the FFT to all of the other non-zero bins, and we can compare how square the precipitates in the two microstructures are by comparing the energy in every fourth non-zero frequency bin (four and eight highlighted in cyan) to the energy in every other non-zero frequency bin. A similar calculation can be performed for 2 Hz energies and all the harmonics. This can detect rafting in microstructures. These three numbers are a quick way to distill microstructure information and compare images in a rotation invariant way. The calculations for the materials from figure 2 are shown in table 2.

It is conceivable that the HOG feature descriptor could be employed to assess elastic anisotropy in a single sample as well, though this is not investigated in this paper.

There are limits to what information the HOG feature descriptor can extract from a microstructure. For instance, if the cuboidal precipitates in the top sample of figure 2 were not globally aligned with each other, then the HOG feature descriptor for that would appear more uniform like that of the bottom sample. This could happen, for example, if the microstructure is from a polycrystalline sample.

The HOG feature descriptor also does not directly reveal information about scale. For instance, it does not say that precipitates in the top sample are on average larger or smaller than the ones in the bottom sample.

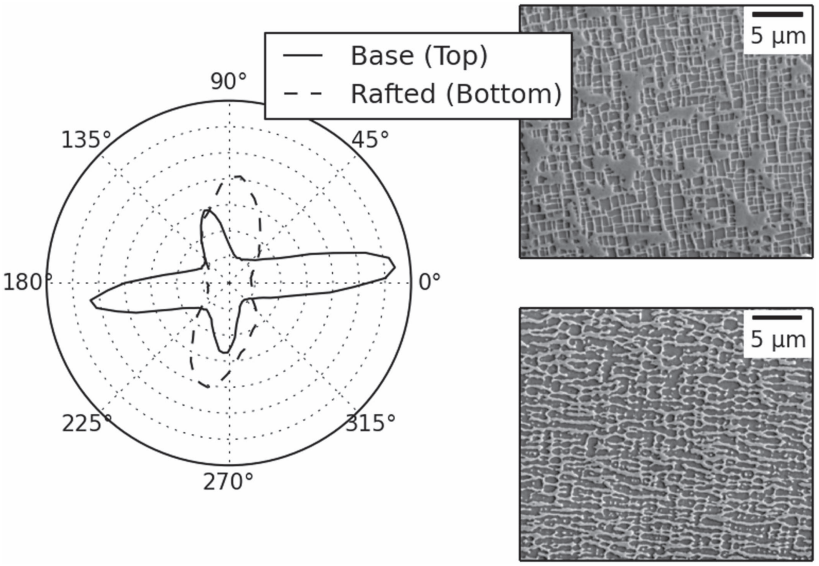

Figure 3. Plot of the HOG feature descriptors of BSE micrographs of a microstructure before (top) and after (bottom) rafting. The rafting is very clear in the HOG feature vector plots. A one pixel blur was used in computing the gradients.

Table 3. These are the simple HOG scores for figure 3. In these two samples, the biggest difference is that the Square score is much higher for the unrafted sample. For the rafted sample, the Square score is lowered but the Layering score remains high.

Simple HOG Scores for figure 3			
	Circle (0 Hz signal)	Square (4 Hz harmonics)	Layering (2 Hz harmonics)
Base (top)	4.4	0.69	0.91
Rafted (bottom)	9.4	0.044	0.98

Taking a step back, even though the microstructures in figure 2 appear to be simple squares and circles, the microstructure samples themselves are 3D objects. It is possible, for instance, that if the top sample was cut on an angle the HOG plot would have more or less peaks due to symmetry and the sectioning plane.

4.2. Detection of rafting

The merits of HOG feature descriptors are easily demonstrated in the context of nickel-based superalloys for rafting, a unique tendency in this class of alloys for the precipitates to directionally coarsen during application of stresses at elevated temperatures [6]. Figure 3 shows two samples of Rene N5, one unrafted (top) and one rafted (bottom) along with plots of their HOG feature vectors. Table 3 shows the FFT-based scores for the rafted microstructure. The biggest change in score from the top (unrafted) microstructure to the bottom (rafted) one is the amount of energy in 4 Hz harmonics. The top microstructure has a large fraction of energy there, and the bottom microstructure has basically none.

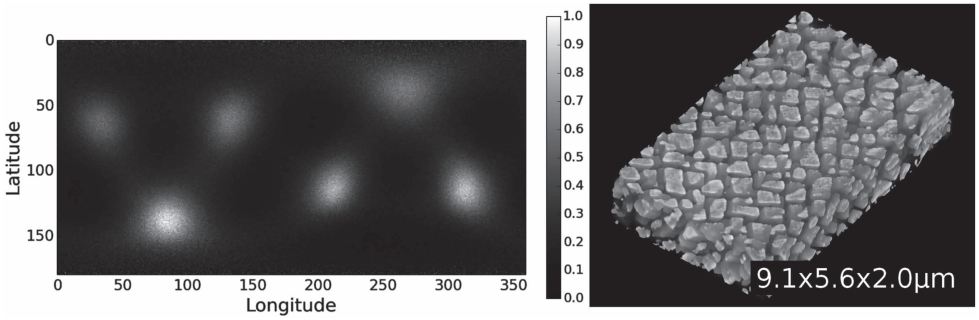

Figure 4. On the left is the 3D HOG descriptor for a 3D BSE dataset (volume rendered on the right) of Rene N4 dataset collected with the Tribeam system [27]. It is the full 3D dataset associated with the image in figure 1, which provides evidence that the HOG descriptor produces easily interpretable results even in the face of large amounts of noise (considerable effort was made to smooth the dataset for the volume rendering).

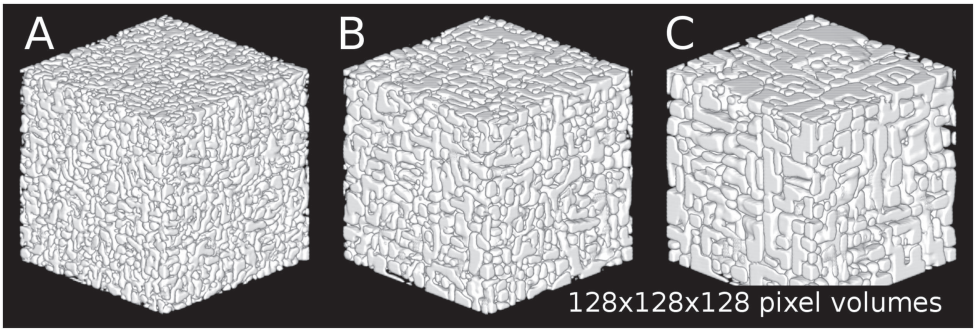

Figure 5. *A* is the base microstructure, *B* is timestep two in the rafting process, and *C* is timestep eight. The data is from the simulations of Wang *et al* [29].

4.3. Analysis of 3D transformations

HOG descriptors easily transfer to 3D datasets as well. While not as extensively deployed as their 2D counterparts, these feature detectors have found practical use in video datasets for action recognition (two spatial dimensions and one time dimension) [26]. Again, in this application, they enable microstructure analysis without segmentation.

Segmentation in 3D datasets can be quite difficult. All of the same problems with 2D data remain, except now visually verifying segmentations is more involved (requiring either volume rendering or a careful use of contour plots).

A 3D HOG is simply a histogram across two-dimensions. For visualization, it is usually desirable to adjust the values in the histogram to account for some bins covering a larger area on the sphere than others so that the values in the histogram are given per-area rather than just as a total sum. This adjustment is used in figure 4 to show a 3D microstructure along with its HOGs plot. As shown in figure 4, there are six distinct peaks corresponding to the 6 faces of the cube-shaped precipitates. Importantly, unlike the 2D analysis, which would return a different shape based on the sectioning plane, the 3D analysis would identify a cube shape regardless of sectioning plane. The clarity of the 3D HOG plot in figure 4 demonstrates the robustness of these feature detectors to noise.

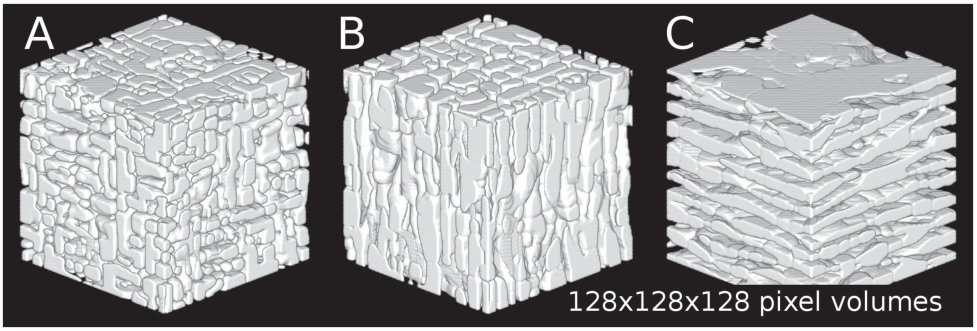

Figure 6. *A* is the base microstructure, *B* is the result of rafting to columns, and *C* is the result of rafting to layers. The data is from the simulations of Wang *et al* [29].

In analogy to the FFTs, it is possible to use rotation invariant spherical harmonics [28] as feature vectors for analysis of 3D microstructures. Figure 5 along with table 4 show the results on a simulated coarsening experiment done by Wang [29]. The first descriptor in table 4 ('Cube') comes from looking at every fourth non-zero frequency bin of the rotation invarient spherical harmonics, and second descriptor ('Sphere') comes from looking at the energy in the zeroth bin compared to everything else. The 'Cube' score remains relatively stable compared to the 'Sphere' score which drops precipitously. This can be explained by thinking about the precipitate edge curvature remaining constant while the edge lengths increase. The precipitates are cuboids through the whole process, they are just becoming less and less spherical as the microstructure coarsens.

Another simpler way to quantify 3D microstructure is to look at the mass moments of inertia of the HOG feature descriptor itself (computed as if the HOG were a thin-shelled spherical object with mass given by the value at each histogram point).

For a cubic microstructure, there are six peaks in the HOG feature descriptor and three equivalent primary axis of rotation in the spherical HOG object. For a microstructure rafted into a columnar structure, there are only four strong peaks in the HOG feature detector, and likewise two equivalent axes of rotation with large moments of inertia and a third with a smaller moment. For a microstructure rafted into a layer by layer structure, the HOG feature detector has only two strong peaks and there is a single large moment of inertia and two smaller ones for the spherical HOG object. Figure 6 shows volume renderings of these two types of rafting that come from simulations done by Wang [29]. Table 5 shows the moment analysis of these experiments which reflects the behavior described above (data also from Wang [29]).

4.4. Effects of sample drift

Other than shot noise, sample drift is another important source of error in scan based imaging techniques. These distortions are most significant with analysis techniques that depend on feature correlations between images, long microscope exposure times, and high magnifications. For a detailed discussion of distortions in scanning electron microscopy, see [30, 31]. For the HOG descriptors used in this paper though, it is hoped that these issues can be largely avoided. First, the descriptors here are not useful for spatially correlating images. Secondly, if image acquisition can be done rapidly relative to the scale of the images acquired, then drift should be minimal. Images collected with faster acquisition times have more shot noise, but

Table 4. The Cube and Sphere scores for these microstructures are computed similarly to the Circle and Square scores from tables 2 and 3.

Coarsening experiment		
Timestep	Cube	Sphere
1	0.71	21.2
2	0.85	7.4
3	0.87	4.0
4	0.87	2.7
5	0.86	2.0
6	0.84	1.6
7	0.83	1.3
8	0.82	1.1
9	0.82	1.0
10	0.81	0.9

Table 5. Moments of the 3D HOG feature descriptor treated as a thin-shell object with density given by the value of the HOG (at each step the total mass of this object is scaled to one). In the columnar rafting experiment, the moments slowly transform from all being equal to two smaller moments (m_1 and m_2) and one large one (m_3). In the layered rafting experiment, the moments slowly transform from being similar to one smaller moment (m_1) and two larger ones (m_2 and m_3).

Moments for HOGs of rafted microstructures						
	Columnar rafting (P-type)			Layered-by-layer rafting (N-type)		
Time	m_1	m_2	m_3	m_1	m_2	m_3
1	0.743	0.745	0.800	0.723	0.784	0.787
2	0.731	0.733	0.823	0.688	0.802	0.804
3	0.721	0.724	0.841	0.656	0.818	0.820
...						
t	0.669	0.671	0.928	0.325	0.949	0.952
$t+1$	0.661	0.664	0.939	0.308	0.954	0.956
$t+2$	0.657	0.659	0.945	0.297	0.957	0.959
$t+3$	0.654	0.655	0.950	0.288	0.969	0.961
$t+4$	0.651	0.653	0.953	0.282	0.960	0.962
$t+5$	0.650	0.651	0.955	0.277	0.962	0.963

the scale of the Gaussian filter in the derivative approximation of the HOG can be adjusted to accommodate for this noise.

If drift cannot be avoided, naturally the HOGs will be affected. To study the types of error that would appear in the HOG descriptors in the presence of drift, the TEM micrographs in figure 2, the BSE micrographs in figure 3, and the simulated data set in figure 5 were all subjected to artificial drift. In the case of the TEM and BSE micrographs, this corresponds directly with sample drift in the microscope. In the case of the 3D simulated data, which is nothing but a stack of 2D slices, this corresponds more closely with errors in registering a 3D stack of images.

For the micrographs in figures 2 and 3, a sequence of shearing distortions were applied that shifted the bottom of the micrograph horizontally some distance with respect to the top. This was done for a range of distortions between zero and five percent of the total width of the images. These experiments were repeated for a vertical shearing distortion of the same length in pixels as the horizontal distortion. For each distortion, the feature descriptors given in tables 2 and 3 were recomputed. The maximum relative error in each of the three feature descriptors with respect to the features computed with the undistorted data was 35% for the Square feature, 9.0% for the Layering feature, and 23% for the Circle feature. We would expect that classifiers based on HOG descriptors should be able to handle these errors, as the values of the feature descriptors that discriminate between images are frequently a factor of five or more different (as is indeed the case in tables 2 and 3).

For the 3D simulated data set in figure 5, a similar set of shear distortions (up to five percent) were tested. For the columnar microstructure, the distortion direction was chosen to be perpendicular to the length of the columns (so the columns leaned to one side) and for the layered microstructure the distortion direction was chosen in the normal direction of the layers (so the layers were no longer level). For each level of distortion, the moments given in table 5 were recomputed. The maximum relative error in each of the three moments with respect to the moments of the undistorted data was 8.2% for the smallest moment, 2.5% for the middle moment, and 1.6% for the largest moment. Similarly to the 2D case, these errors do not change the conclusions of the analysis of table 5 (the errors in the largest moments are most important, and they are smallest).

5. Conclusion

This paper demonstrates that in many types of basic microstructure analysis it is possible to employ an HOGs feature vector in place of difficult to compute segmentation statistics. While the HOG has limitations, it is easy to compute and is more robust to common noise sources in electron microscopy techniques and can be applied in a number of interesting applications in both 2D and 3D datasets.

Acknowledgments

The BSE micrographs in figure 3 come from data collected by Luke Rettenberg. This material is based upon work supported by the National Science Foundation under Grants No. DMR 1233704 and DMR 1534264.

References

[1] Echlin M P, Lenthe W C and Pollock T M 2014 Three-dimensional sampling of material structure for property modeling and design *Integr. Mater. Manuf. Innov.* **3** 1–14
[2] Callahan P G, Simmons J P and De Graef M 2013 A quantitative description of the morphological aspects of materials structures suitable for quantitative comparisons of 3D microstructures *Modelling Simul. Mater. Sci. Eng.* **21** 015003
[3] Callahan P G and Graef M D 2012 Precipitate shape fitting and reconstruction by means of 3D Zernike functions *Modelling Simul. Mater. Sci. Eng.* **20** 015003
[4] Sluytman J V and Pollock T 2012 Optimal precipitate shapes in nickel-base alloys *Acta Mater.* **60** 1771–83
[5] Underwood E E 1973 Quantitative stereology for microstructural analysis *Microstructural Analysis: Tools and Techniques* (Boston, MA: Springer) pp 35–66

[6] Tin S, Pollock T and King W 2000 Carbon additions and grain defect formation in high refractory nickel-base single crystal superalloys *Superalloys 2000* (Warrendale, PA: TMS) p 201–9
[7] Comer M, Bouman C A, Graef M and Simmons J P 2011 Bayesian methods for image segmentation *JOM* **63** 55–7
[8] Simmons J, Bartha B, De Graef M and Comer M 2008 Development of Bayesian segmentation techniques for automated segmentation of titanium alloy images *Microsc. Microanal.* **14** 602–3
[9] Gulsoy E and De Graef M 2009 Advances in the automated segmentation of 3-D microstructures *Microsc. Microanal.* **15** 606–7
[10] Huffman L, Simmons J, Graef M D and Pollak I 2011 Shape priors for map segmentation of alloy micrographs using graph cuts *2011 IEEE Statistical Signal Processing Workshop (SSP)* pp 661–4
[11] Chaudhuri B, Kundu P and Sarkar N 1993 Detection and gradation of oriented texture *Pattern Recognit. Lett.* **14** 147–53
[12] Dalal N and Triggs B 2005 Histograms of oriented gradients for human detection *IEEE Computer Society Conf. on Computer Vision and Pattern Recognition, 2005. CVPR 2005* vol 1, pp 886–93
[13] Felzenszwalb P F, Girshick R B, McAllester D and Ramanan D 2010 Object detection with discriminatively trained part-based models *IEEE Trans. Pattern Anal. Mach. Intell.* **32** 1627–45
[14] Fährmann M, Fratzl P, Paris O, Fährmann E and Johnson W C 1995 Influence of coherency stress on microstructural evolution in model Ni–Al–Mo alloys *Acta Metall. Mater.* **43** 1007–22
[15] Gabb T, Kantzos P, Telesman J, Gayda J, Sudbrack C and Palsa B 2011 Fatigue resistance of the grain size transition zone in a dual microstructure superalloy disk *Int. J. Fatigue* **33** 414–26
[16] Stegmann M B and Gomez D D 2002 A brief introduction to statistical shape analysis *Informatics and Mathematical Modelling* DTU 15 Technical University of Denmark
[17] Belongie S, Malik J and Puzicha J 2002 Shape matching and object recognition using shape contexts *IEEE Trans. Pattern Anal. Mach. Intell.* **24** 509–22
[18] Lowe D G 1999 Object recognition from local scale-invariant features *Proc. 7th IEEE Int. Conf. on Computer Vision, 1999* vol 2, pp 1150–7
[19] Dalal N and Triggs B 2005 Histograms of oriented gradients for human detection *2005 IEEE Computer Society Conf. on Computer Vision and Pattern Recognition (CVPR'05)* vol 1, pp 886–93
[20] Krizhevsky A, Sutskever I and Hinton G E 2012 Imagenet classification with deep convolutional neural networks *Advances in Neural Information Processing Systems* pp 1097–105
[21] Faber E, Martinez-Martinez D, Mansilla C, Ocelík V and Hosson J D 2015 Calibration-free quantitative surface topography reconstruction in scanning electron microscopy *Ultramicroscopy* **148** 31–41
[22] Mansilla C, Novais M H, Faber E, Martínez-Martínez D and Hosson J T De 2016 On the 3d reconstruction of diatom frustules: a novel method, applications, and limitations *J. Appl. Phycol.* **28** 1097–110
[23] Fullwood D T, Niezgoda S R and Kalidindi S R 2008 Microstructure reconstructions from 2-point statistics using phase-recovery algorithms *Acta Mater.* **56** 942–8
[24] Niezgoda S R, Turner D M, Fullwood D T and Kalidindi S R 2010 Optimized structure based representative volume element sets reflecting the ensemble-averaged 2-point statistics *Acta Mater.* **58** 4432–45
[25] DeCost B L and Holm E A 2015 A computer vision approach for automated analysis and classification of microstructural image data *Comput. Mater. Sci.* **110** 126–33
[26] Klaser A, Marszalek M and Schmid C 2008 A Spatio-temporal descriptor based on 3D-gradients *BMVC 2008-19th British Machine Vision Conf.* ed M Everingham *et al* (United Kingdom: British Machine Vision Association, Leeds) pp 275:1–10
[27] Echlin M P, Mottura A, Wang M, Mignone P J, Riley D P, Franks G V and Pollock T M 2014 Three-dimensional characterization of the permeability of W-Cu composites using a new 'TriBeam' technique *Acta Mater.* **64** 307–15
[28] Kazhdan M, Funkhouser T and Rusinkiewicz S 2003 Rotation invariant spherical harmonic representation of 3d shape descriptors *Proc. 2003 Eurographics/ACM SIGGRAPH Symp. on Geometry Processing, SGP '03 (Eurographics Association, Aire-la-Ville, Switzerland)* pp 156–64 http://dl.acm.org/citation.cfm?id=882370.882392
[29] Zhou N, Shen C, Mills M and Wang Y 2010 Large-scale three-dimensional phase field simulation of γ'-rafting and creep deformation *Phil. Mag.* **90** 405–36

[30] Kammers A D and Daly S 2013 Digital image correlation under scanning electron microscopy: methodology and validation *Exp. Mech.* **53** 1743–61
[31] Mansilla C, Ocelík V and Hosson J T M D 2014 A new methodology to analyze instabilities in sem imaging *Micros. Microanal.* **20** 1625–37